Materials Horizons

ROYAL SOCIETY OF CHEMISTRY

COMMUNICATION

View Article Online
View Journal

Check for updates

Cite this: DOI: 10.1039/d6mh00453a

Received 10th March 2026,
Accepted 7th April 2026

DOI: 10.1039/d6mh00453a

rsc.li/materials-horizons

Published on 07 April 2026. Downloaded by NANJING UNIVERSITY on 5/12/2026 11:44:42 AM.

Harnessing weak monomer miscibility to create porous microdomains in polymer electrolytes for zinc-ion batteries

Lei Zhang,[ab] Shijun Xiao,[b] Xurui Rong,[a] Zhiheng Shao,[a] Yong Jiang,[a] Jiajun Hu,[a] Wenyu Wang,[a] Gangling Chen,[a] Jitao Huang,*[ce] Qian Wang,*[d] Zhong Jin *[c] and Shi Wang *[abc]

The practical deployment of aqueous zinc-ion batteries is fundamentally constrained by rampant dendrite growth and parasitic reactions at the anode. To address this, we design an amphiphilic ionogel electrolyte *via* molecular engineering. The material is synthesized by copolymerizing acrylamide and 2,2,3,4,4,4-hexafluorobutyl acrylate in a zinc salt/ionic liquid medium. During polymerization, *in situ* phase separation is triggered by the differing solubility of the two polymer components, followed by water-induced self-assembly driven by hydrophilic/hydrophobic interactions. This process ultimately yields gradient pore channels that enable fast and uniform Zn^{2+} transport. More importantly, the amphiphilic components synergistically modulate the interface: hydrophilic polyacrylamide chains anchor onto the zinc, immobilizing water and regulating solvation, while hydrophobic fluorinated domains form a barrier that excludes water and offers supplemental Zn^{2+} coordination. Consequently, the ionogel enables rapid, uniform zinc deposition, reduces the nucleation barrier, and promotes a robust fluoride- and Zn_3N_2-rich hybrid interphase. A Zn||Zn symmetric cell achieves stable cycling for over 2800 hours at 2 mA cm^{-2}, and a full cell with a $Na_2V_6O_{16}{\cdot}3H_2O$ cathode maintains a high capacity above 350 mAh g^{-1} with prolonged cyclability. This work demonstrates a molecular-level design strategy for electrolyte matrices that simultaneously guide ion flux and tailor interfacial chemistry, providing a pathway towards durable metal batteries.

New concepts

This work introduces a paradigm shift in electrolyte design through a molecularly engineered amphiphilic ionogel with a biomimetic gradient pore architecture, constructed *via in situ* phase separation driven by differential monomer solubility followed by water-induced self-assembly. This unique structure serves as an active ion redistributor, homogenizing Zn^{2+} flux prior to deposition. The conceptual leap lies in orchestrating a molecular "division of labor" at the interface: hydrophilic segments anchor to regulate solvation, while hydrophobic fluorinated domains form a protective water-excluding barrier. This synergy between structural gradients and chemical asymmetry enables a robust hybrid interphase and preferred crystallographic orientation, establishing a generalizable blueprint for stabilizing multivalent metal anodes.

Introduction

Rechargeable aqueous zinc-ion batteries have emerged as promising candidates for large-scale energy storage due to the intrinsic safety, low cost, and high theoretical capacity of zinc metal.[1–4] However, the practical deployment of this technology is persistently hampered by the poor reversibility of the zinc anode.[5–7] Uncontrolled dendritic growth during plating and a cascade of parasitic reactions—including hydrogen evolution, corrosion, and passivation—lead to rapid capacity fade, short circuiting, and ultimately, cell failure.[8–11] The origin of these issues is deeply rooted in the heterogeneous ionic flux at the electrode–electrolyte interface and the high activity of water molecules in conventional aqueous electrolytes.

---

[a] School of Materials and Chemical Engineering, Chuzhou University, Chuzhou 239099, China. E-mail: iamshiwang@njupt.edu.cn

[b] State Key Laboratory of Flexible Electronics (LoFE) & Institute of Advanced Materials (IAM), Nanjing University of Posts & Telecommunications, 9 Wenyuan Road, Nanjing 210023, China

[c] State Key Laboratory of Coordination Chemistry, MOE Key Laboratory of Mesoscopic Chemistry, MOE Key Laboratory of High Performance Polymer Materials and Technology, Jiangsu Key Laboratory of Green Energy Catalysis and Intelligent Chemical Engineering, Suzhou Key Laboratory of Green Intelligent Manufacturing of New Energy Materials and Devices, Tianchang New Materials and Energy Technologies Research Center, Institute of Green Chemistry and Engineering, School of Chemistry and Chemical Engineering, Nanjing University, Nanjing, Jiangsu, 210023, China. E-mail: zhongjin@nju.edu.cn

[d] College of Materials Science and Engineering, Taiyuan University of Technology, Taiyuan, 030024, China. E-mail: qianwang0825@pku.edu.cn

[e] College of New Energy and Materials, Ningde Normal University, Ningde, 352100, China

Published on 07 April 2026. Downloaded by NANJING UNIVERSITY on 5/12/2026 11:44:42 AM.

Substantial research efforts have been directed towards electrolyte engineering to stabilize zinc electrodeposition.[12] Strategies such as high-concentration salt electrolytes,[13,14] hydrogel polymers,[15–17] and organic additive formulations[18–20] have shown promise in modulating Zn^{2+} solvation structure and suppressing water activity. Nonetheless, these approaches often face inherent trade-offs. High salt concentrations increase cost and viscosity;[21,22] hydrogels may suffer from insufficient mechanical robustness or low zinc-ion transference number;[23] while additives can be progressively consumed.[24] Crucially, most existing designs focus on either bulk electrolyte properties or homogeneous interfacial modification, lacking the spatial gradation to simultaneously manage ion transport kinetics from the electrolyte bulk to the deposition plane and precisely engineer the interfacial microenvironment.[25,26] An ideal electrolyte matrix should therefore integrate *graded* ion-conducting pathways to homogenize Zn^{2+} flux *en route* to the electrode,[27] coupled with *asymmetric* interfacial chemistry to selectively regulate the deposition process and shield the anode from water.

Drawing inspiration from functional gradients and molecular self-assembly in natural systems, we designed an amphiphilic ionogel electrolyte with a gradient porous architecture to simultaneously meet these dual requirements. This structure is constructed through the copolymerization of acrylamide and a fluorinated monomer in an ionic liquid/zinc salt medium, where *in situ* phase separation occurs during polymerization, followed by controlled water immersion to drive hydrophilic/hydrophobic self-assembly of the polymer chains. The resulting pore-size gradient functions as an effective built-in ion redistributor within the electrolyte. More innovatively, the amphiphilic nature of the copolymer orchestrates a molecular-scale ‘‘division of labor’’ at the zinc interface: hydrophilic polyacrylamide segments anchor to the surface to manage solvation, while hydrophobic fluorinated chains spontaneously form an outer shield to exclude active water and provide supplementary ion-coordination sites. This synergistic design enables the formation of a robust, hybrid solid–electrolyte interphase (SEI) and facilitates uniform deposition with a preferred crystal orientation. The presented electrolyte demonstrates exceptional performance in stabilizing symmetric Zn||Zn cells and enabling high-capacity, long-cycle-life full batteries. This study provides a paradigm of spatially and chemically coordinated electrolyte design, offering a generalizable pathway to overcome interfacial instability in metal anode-based batteries.

Results and discussion

To fabricate an amphiphilic ionogel with graded zinc-ion migration pathways, the material was synthesized *via* copolymerization of the fluorinated monomer 2,2,3,4,4,4-hexafluorobutyl acrylate (HFBA) and acrylamide in the presence of a suitable amount of the ionic liquid (1-ethyl-3-methylimidazolium bis(trifluoromethylsulfonyl)imide, [EMIm]TFSI) and zinc salt. Detailed synthesis procedures are provided in the Supplementary Information. [EMIm]TFSI acts as a solvent that poorly dissolves acrylamide and its polymer (PAAm), but exhibits good solubility toward fluorinated monomer and polymer. This disparity in solubility induces *in situ* phase separation within the electrolyte membrane, leading to the formation of ion-conducting channels impregnated with zinc salt. Limited water was added to the as-prepared membrane to yield the final ionogel. This water-introduction step further enhances zinc-ion mobility. Meanwhile, the hydrophilic nature of PAAm and the hydrophobic character of the fluorinated polymer drive a self-assembly process that finely tunes the phase-separated morphology. The water content was systematically optimized at approximately 20 wt%, balancing sufficient hydration to promote Zn^{2+} mobility with the preservation of structural integrity and hydrophobic barrier function. This water level also proves critical for driving the subsequent hydrophilic/hydrophobic self-assembly that establishes the gradient pore architecture.

Consequently, phase-separated pores ranging from large to small is formed, thereby establishing a gradient in the zinc-ion migration pathways. Fig. 1a further illustrates the operating mechanism of this amphiphilic ionogel. Solvated zinc ions first coordinate with the fluorine-containing groups in the fluorinated monomer *via* ion–dipole interactions, which lowers the desolvation energy barrier. The zinc ions then hop toward oxygen-functional groups and migrate to the interface. At the interface, which is rich in polyacrylamide segments, water molecules form hydrogen bonds with $-NH_2$ groups and become immobilized, significantly promoting zinc-ion desolvation. Thereafter, the zinc ions continue to coordinate with oxygen species and migrate uniformly through the channels until deposition onto the zinc electrode surface. This process collectively suppresses hydrogen evolution and corrosion, while guiding uniform zinc deposition.

Fig. 1b compares the mechanical properties of the amphiphilic ionogel electrolyte (denoted as PBAM-IL-Zn) and a polyacrylamide-based ionogel electrolyte (denoted as PAM-IL-Zn) prepared under identical conditions. The PBAM-IL-Zn exhibits a fracture elongation exceeding 900% and a fracture strength over 0.8 MPa, substantially higher than those of PAM-IL-Zn ($\sim$700% elongation and $\sim$0.43 MPa strength). This enhancement is primarily attributed to the random copolymer structure, which comprises poorly soluble polyacrylamide segments and highly soluble fluorinated polymer components. These respective phases form a poorly solvated domain (reinforced by hydrogen bonds, imparting rigidity) and a highly solvated domain (dominated by ionic interactions, providing elasticity), synergistically toughening the ionogel. In essence, the one-step random copolymerization simultaneously creates two distinct domains within the ionogel responsible for stretchability and stiffness, thereby yielding an ionogel with high strength and high extensibility (It should be noted that the presence of approximately 20% water in the ionogel also contributes to its final mechanical properties, although this is not the dominant factor). The high stretchability of the ionogel is further demonstrated in Fig. 1c and Fig. S1.

Fig. 1d–f present the microstructural morphology of PBAM-IL-Zn characterized by SEM. As shown in Fig. 1d, distinct microphase separation is observed on the surface of the

This journal is © The Royal Society of Chemistry 2026

Published on 07 April 2026. Downloaded by NANJING UNIVERSITY on 5/12/2026 11:44:42 AM.

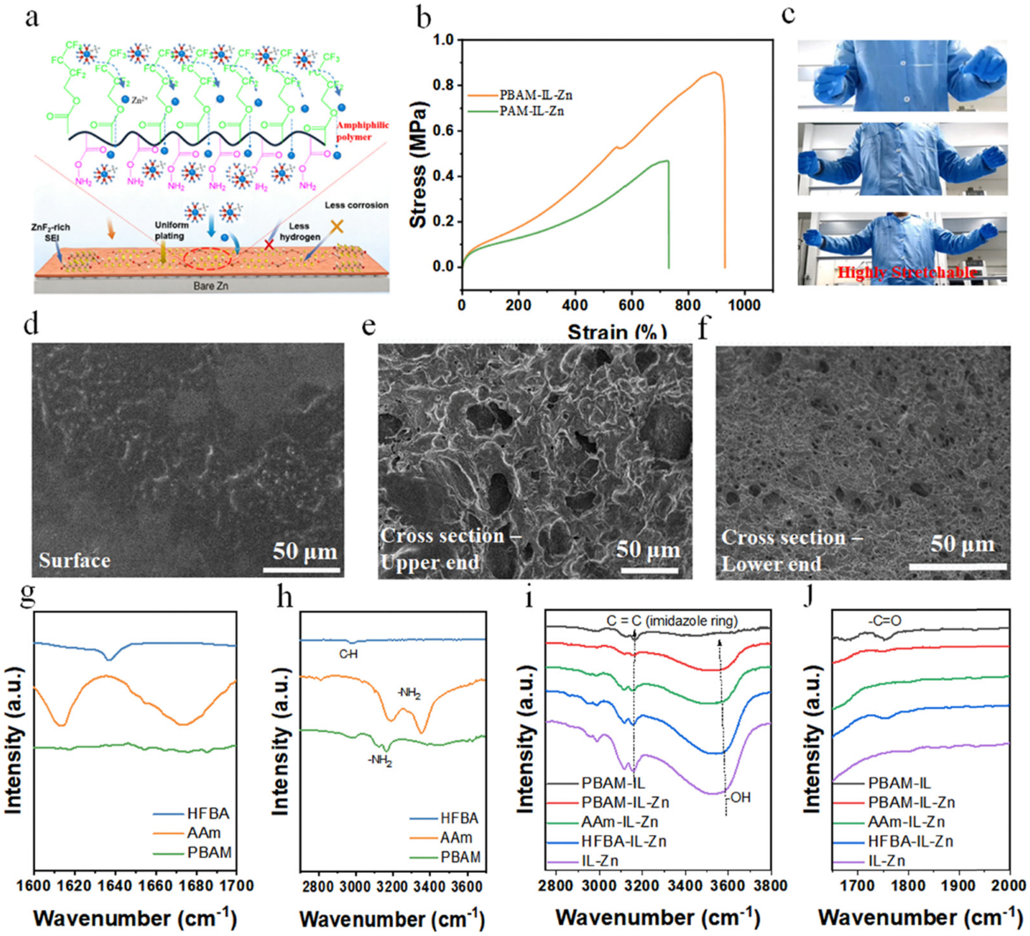

Fig. 1 Mechanism, mechanical properties, and morphological characterization of the amphiphilic ionogel. (a) Structure of the amphiphilic ionogel, its solvation structure, and the interfacial regulation mechanism. (b) Stress–strain curve and (c) photographs under stretching of the ionogels (PBAM-IL-Zn and PAM-IL-Zn). SEM images of PBAM-IL-Zn: (d) surface, (e) upper cross-sectional region, and (f) lower cross-sectional region. (g)–(j) FTIR characterization of the series of samples.

membrane, confirming the earlier proposed mechanism, which evidently arises from the differential solubility of the polymer chains. In cross-sectional views, larger phase-separated pores are evident in the upper region of the membrane (Fig. 1e), while the lower region exhibits smaller phase-separated pores (Fig. 1f). This gradient in pore size is attributed to the further self-assembly induced by the introduction of water molecules. Consequently, the electrolyte membrane forms a structure with graded phase-separated channels, which serve as zinc-ion migration pathways. In contrast, PAM shows no obvious gradient porous structure, further confirming the significant advantage of amphiphilic copolymers in the regulation of microstructure (Fig. S2).

Further structural and interactional insights into the ionogels were obtained through infrared (IR) spectroscopy. Fig. 1g displays the IR spectra of the monomers (HFBA and AAm), and the polymer PBAM. The characteristic C═C stretching peaks in the range of 1600–1700 cm^{-1}, present in the monomers, disappear in the polymer spectrum, confirming successful polymerization. In Fig. 1h, the prominent dual peaks at 3179 and 3359 cm^{-1} in the AAm monomer, assigned to the N–H stretching of the –NH$_2$ group, redshift to 3121 and 3166 cm^{-1} upon incorporation of HFBA. This shift is attributed to hydrogen bonding interactions between the –NH$_2$ groups and the fluorine-containing moieties. To investigate the influence of polymer composition on the Zn^{2+} solvation structure, corresponding IR spectra were analyzed. As shown in Fig. 1i, the –OH stretching peak of water molecules in the IL-Zn electrolyte exhibits a slight redshift upon the addition of HFBA. A more pronounced redshift is observed when AAm is introduced. This clearly indicates that hydrogen bonding between the –NH$_2$ groups of AAm and water disrupts the original Zn^{2+} solvation structure. While the –CF$_3$ groups in HFBA also interact with water, this interaction is weaker than the direct hydrogen bonding from AAm, resulting in a smaller spectral shift. Overall, the combined effect of both functional groups in the PBAM polymer leads to the most significant –OH redshift, indicating a synergistic disruption of the solvation sheath. This facilitates greater incorporation of IL into the Zn^{2+} solvation structure, thereby reducing the content of active water. Correspondingly, the characteristic peak of the imidazolium ring double bond is notably affected and redshifts due to the increased anion

Published on 07 April 2026. Downloaded by NANJING UNIVERSITY on 5/12/2026 11:44:42 AM.

participation in the solvation shell. Furthermore, as shown in Fig. 1j, the –C═O stretching peak of the polymer backbone, appearing at 1754 cm^{-1} in PBAM-IL, undergoes a distinct redshift to 1750 cm^{-1} in PBAM-IL-Zn. This provides strong evidence for coordination between the carbonyl oxygen and Zn^{2+}, offering an additional pathway for efficient zinc-ion migration. The IR spectrum in Fig. S2 shows a clear blueshift of the characteristic $-CF_2-$ stretching vibration from the fluorinated polymer chains. This can be ascribed to coordination between the electronegative fluorine atoms and Zn^{2+}, which is also favorable for rapid zinc-ion transport.

To investigate the relationship between the ionic conductivity of the PBAM-based ionogel and the zinc salt content, three PBAM electrolytes with different compositions were prepared by varying the mass of $Zn(OTf)_2$ (0.5 g, 0.75 g, and 1.0 g) while keeping the amounts of monomers and ionic liquid constant. The electrochemical impedance spectroscopy (EIS) results for these ionogels are presented in Fig. 2a. PBAM-IL-Zn-0.75 exhibited the lowest bulk resistance (7.2 Ω), whereas PBAM-IL-Zn-1.0 and PBAM-IL-Zn-0.5 showed significantly higher resistances of 35.3 Ω and 45.9 Ω, respectively. The corresponding room-temperature ionic conductivities were calculated to be 8.8 mS cm^{-1}, 1.23 mS cm^{-1}, and 1.6 mS cm^{-1}. This trend suggests that at low salt concentrations, the number of charge carriers is limited, while excessively high salt concentrations may exceed the solubility limit and cause ionic crowding, both of which impede ion transport. Based on these results, PBAM-IL-Zn-0.75 (which is the PBAM-IL-Zn discussed in the previous section) was selected as the optimal composition for subsequent studies. To evaluate the impact of HFBA incorporation on Zn^{2+} transport, the ionic transference number was determined *via* chronoamperometry (potentiostatic polarization). The current–time curves (and corresponding EIS spectra before and after polarization) for PBAM-IL-Zn and PAM-IL-Zn are shown in Fig. 2c and Fig. S4, respectively. PBAM-IL-Zn achieved a significantly higher Zn^{2+} transference number (0.47) compared to PAM-IL-Zn (0.13). This enhancement is attributed to the synergistic effects of the amphiphilic ionogel's unique structure: The F and O moieties provide coordination sites for Zn^{2+}, the $-NH_2$ groups immobilize water molecules to promote desolvation, and the graded microphase separation establishes a gradient ion-conduction pathway.

Furthermore, the temperature-dependent interfacial resistance of Zn||Zn symmetric cells (Fig. 2d) was analyzed to

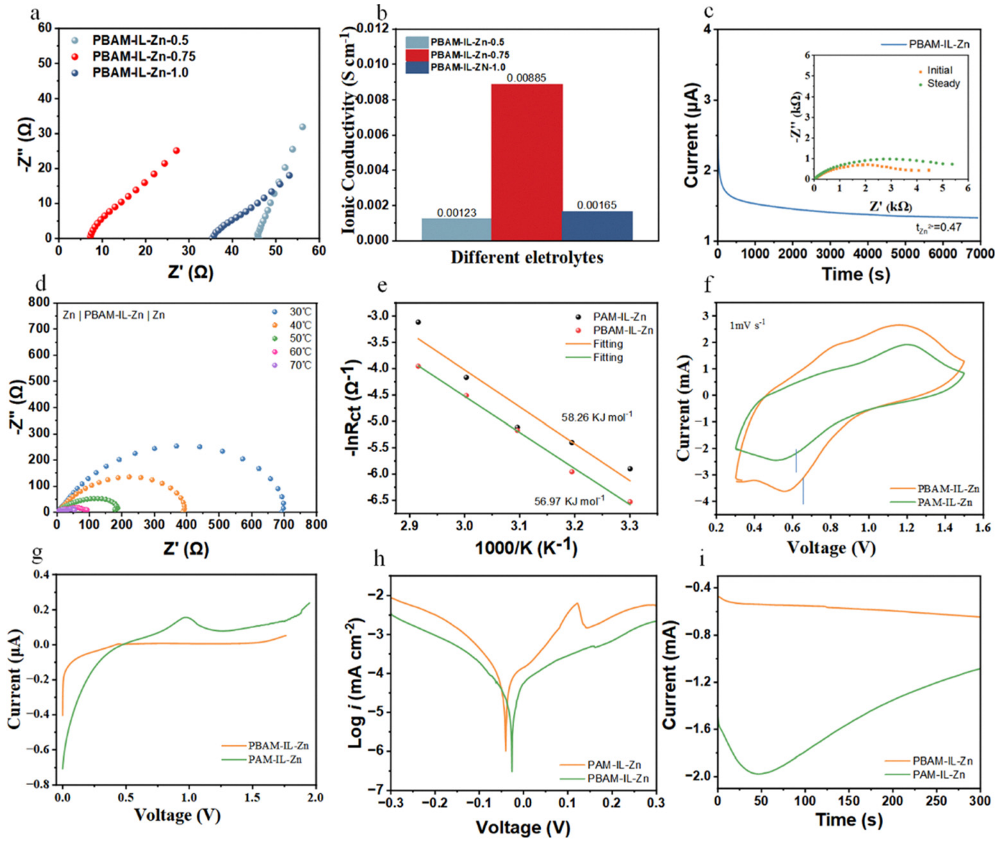

Fig. 2 Electrochemical performance characterization of the electrolyte membrane. (a) EIS characterization and (b) corresponding room-temperature ionic conductivity of PBAM-based electrolytes with different zinc salt contents. (c) Polarization curve and EIS profiles before and after polarization for the Zn|PBAM-IL-Zn|Zn symmetric cell. (d) EIS of the Zn|PBAM-IL-Zn|Zn symmetric cell at various temperatures. (e) Relationship between interfacial resistance and temperature for symmetric Zn||Zn cells employing PAM-IL-Zn and PBAM-IL-Zn at different temperatures. (f) CV curves of full cells using PAM-IL-Zn and PBAM-IL-Zn. (g) LSV, (h) Tafel plots, and (i) chronoamperometric test at a constant voltage of −150 mV for cells based on PAM-IL-Zn and PBAM-IL-Zn.

Published on 07 April 2026. Downloaded by NANJING UNIVERSITY on 5/12/2026 11:44:42 AM.

estimate the desolvation energy barrier. As shown in the Arrhenius plot (Fig. 2e), PBAM-IL-Zn exhibits a relatively low desolvation activation energy of 56.97 kJ mol^{-1}. Interestingly, the Nyquist plots of Zn||Zn cells with PAM-IL-Zn electrolyte (Fig. S5) showed lower interfacial resistances (357, 224, 168, 67, and 24 Ω at 30, 40, 50, 60, and 70 °C, respectively) compared to those with PBAM-IL-Zn (692, 388, 187, 85, and 53 Ω at the same temperatures). This difference is likely due to the hydrophobic nature of the fluorinated segments in PBAM-IL-Zn, which forms a barrier layer increasing the internal impedance. This characteristic is beneficial in full-cell configurations, as it can suppress the dissolution and shuttle of cathode active materials, which is corroborated by the cycling performance discussed later. Cyclic voltammetry (CV) of Zn||$Na_2V_6O_{16}\cdot 3H_2O$ (Zn||NVO) full cells was performed to assess the reaction kinetics. As shown in Fig. 2f, the reduction peak potential for the Zn|PBAM-IL-Zn|NVO cell is 0.565 V, which is higher than that of the Zn|PAM-IL-Zn|NVO cell (0.507 V). This positive shift indicates faster Zn^{2+} insertion kinetics and more uniform zinc deposition facilitated by the amphiphilic ionogel.

Fig. 2g shows the linear sweep voltammetry (LSV) curves of the ionogels. The LSV profile for PAM-IL-Zn exhibits significant fluctuations, indicating its limited electrochemical oxidation stability. During charging, the decomposition of free water can occur, leading to hydrogen evolution and consequent battery performance degradation. In contrast, the fabricated PBAM-IL-Zn demonstrates a high anodic stability, tolerating potentials up to 1.75 V (Fig. 2g). This enhanced stability is attributed to the introduction of fluorinated polymer segments, which lowers the highest occupied molecular orbital (HOMO) energy level of the overall polymer matrix. Furthermore, the amphiphilic nature of the polymer reduces the decomposition of free water. These combined effects improve the stability of the zinc anode, thereby contributing to the extended cycle life and higher discharge capacity of the battery.

In aqueous electrolytes, zinc metal anodes are susceptible to corrosion by free water, which severely compromises their cycling lifespan and overall battery performance. To evaluate the corrosion resistance afforded by the electrolytes, Tafel polarization measurements were conducted. As shown in Fig. 2h, the corrosion potential for PBAM-IL-Zn is −0.026 V, which is more positive than that of PAM-IL-Zn (−0.040 V). This result further confirms that the amphiphilic ionogel enhances anode stability through the synergistic regulation of its structure and micro-morphology. Additionally, the corrosion current density for PBAM-IL-Zn is lower than that for PAM-IL-Zn. This indicates that once corrosion initiates, zinc grains formed in PAM-IL-Zn are prone to rapid side reactions, accelerating electrolyte consumption and eventual cell failure. To probe the Zn^{2+} deposition behavior on the zinc anode, chronoamperometry tests were performed using symmetric Zn||Zn cells. As depicted in Fig. 2i, for the cell with PBAM-IL-Zn, the current density shows a transient increase after approximately 25 s before stabilizing. This response suggests that surface two-dimensional (2D) diffusion is restricted, promoting a shift toward three-dimensional (3D) diffusion across the anode surface. This mode favors the formation of uniform and dense zinc deposits, thereby suppressing the growth of disordered zinc dendrites. In contrast, the current response in the PAM-IL-Zn cell remains unstable throughout the deposition process, indicating a dominant 2D diffusion mode that leads to inhomogeneous zinc deposition and consequent degradation of battery performance.

Zn||Cu cells were employed to further assess the influence of the amphiphilic ionogel on the Zn^{2+} deposition/stripping behavior. First, the galvanostatic electrodeposition of Zn onto a Cu substrate was examined at a current density of 7 mA cm^{-2} and a capacity of 7 mAh cm^{-2} to evaluate the Zn^{2+} nucleation characteristics (Fig. 3a). The Zn||PBAM-IL-Zn||Cu cell exhibited a lower nucleation overpotential of only 32.1 mV compared to its Zn||PAM-IL-Zn||Cu counterpart. This result further confirms that the synergistic effects arising from the F/O coordination sites within the polymer matrix and the graded ion-transport channels of the amphiphilic ionogel effectively reduce the nucleation barrier for Zn^{2+}. Consequently, Zn^{2+} requires less energy to penetrate the SEI layer, promoting uniform deposition, accelerating deposition kinetics, and thereby mitigating side reactions, corrosion of the zinc metal electrode, and hydrogen evolution. These findings are in agreement with the results presented in Fig. 2.

Additionally, long-term cycling Coulombic efficiency (CE) tests were conducted for both PBAM-IL-Zn and PAM-IL-Zn electrolytes at 0.5 mA cm^{-2} and 0.5 mAh cm^{-2}. As shown in Fig. S6a, the Zn||PBAM-IL-Zn||Cu half-cell demonstrated stable cycling over 600 cycles with an average Coulombic efficiency of 99.2%. In contrast, the Zn||PAM-IL-Zn||Cu half-cell sustained stable operation for only 250 cycles (Fig. S6b). This further verifies that the amphiphilic ionogel stabilizes the zinc anode, improves the cell's cycling lifespan, and alleviates the issue of side reactions on the zinc metal electrode.

To evaluate the stabilization effect of the ionogel on the zinc metal anode during repeated plating and stripping, Zn||Zn symmetric cells were assembled and tested under various current densities. Fig. 3b presents the rate performance of these cells. Compared to PAM-IL-Zn, PBAM-IL-Zn exhibits lower overpotentials at all tested current densities, indicating faster interfacial reaction kinetics. This observation aligns with the conclusion drawn from Fig. 3a. Furthermore, no abrupt voltage increases were observed in the Zn||Zn cell employing PBAM-IL-Zn, suggesting good compatibility between the electrolyte and the zinc anode without side reactions that would increase internal resistance. Long-term cycling performance further highlights the advantage of PBAM-IL-Zn. As shown in Fig. 3c, under a current density of 0.5 mA cm^{-2} and a capacity of 0.5 mAh cm^{-2}, the voltage profile for the Zn|PAM-IL-Zn|Zn cell became irregularly fluctuating after 100 h of cycling. This is attributed to the continuous growth of zinc dendrites piercing the PAM-IL electrolyte and/or the gradual consumption of the electrolyte, leading to internal short circuits and increased resistance. In contrast, the Zn||Zn cell based on PBAM-IL-Zn maintained stable cycling for over 1200 h under identical conditions, with a stable voltage polarization of approximately

Published on 07 April 2026. Downloaded by NANJING UNIVERSITY on 5/12/2026 11:44:42 AM.

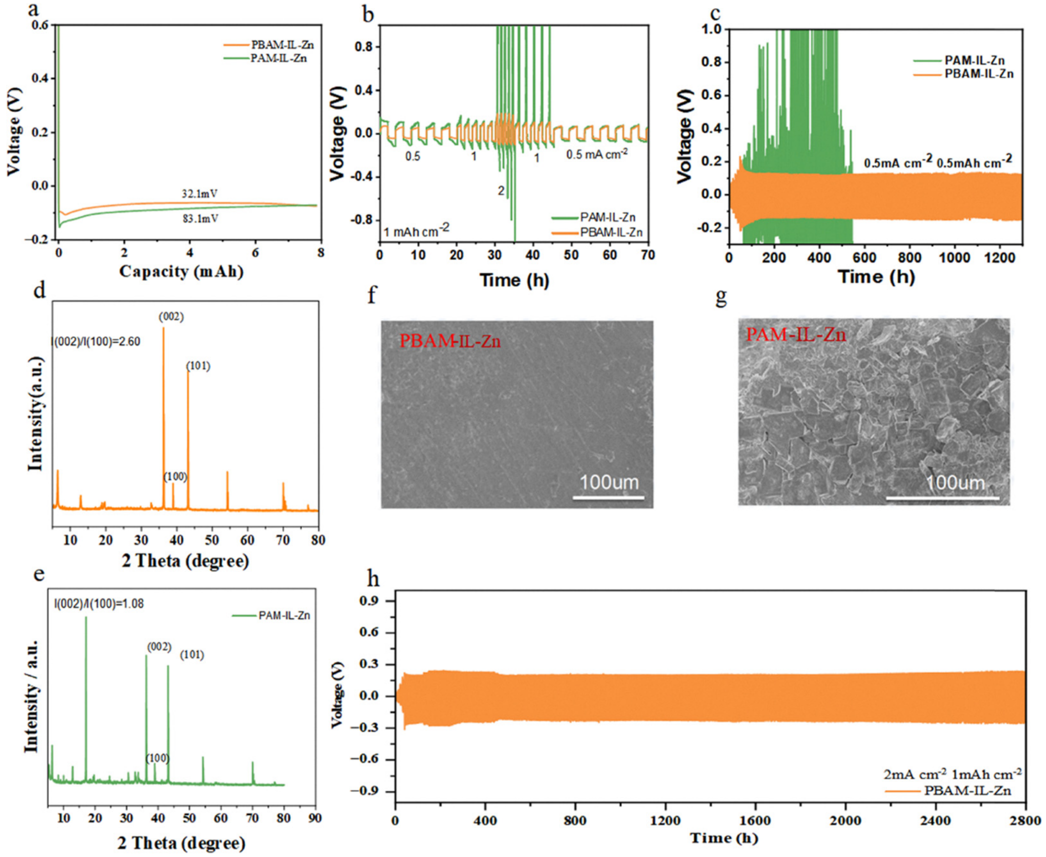

Fig. 3 Nucleation Behavior of Zn||Zn Cells. (a) Initial deposition voltage profiles for cells based on PAM-IL-Zn and PBAM-IL-Zn. (b) Rate performance and (c) Long-term cycling performance of the Zn||Zn batteries. (d)–(e) XRD patterns of the zinc surface and (f)–(g) corresponding SEM characterization after cycling of symmetric Zn||Zn cells. (h) Long-term cycling performance of the symmetric Zn||Zn battery based on PBAM-IL-Zn.

120 mV. This demonstrates the excellent compatibility of PBAM-IL-Zn with the zinc metal electrode, effectively suppressing the formation and growth of dendrites during zinc deposition and stripping.

Post-cycling XRD characterization of the zinc anodes revealed an $I_{(002)}/I_{(101)}$ intensity ratio of 2.60 for the anode cycled with PBAM-IL-Zn (Fig. 3d), significantly higher than the ratio of 1.06 for the anode cycled with PAM-IL-Zn (Fig. 3e). This indicates that PBAM-IL-Zn promotes preferential zinc deposition along the (002) crystal plane. SEM characterization further confirmed a more uniform and dendrite-free surface on the zinc anode cycled with PBAM-IL-Zn (Fig. 3f and g). Similar results were obtained for symmetric cells tested at 0.75 mA cm^{-2} and 0.75 mAh cm^{-2} (Fig. S7).

Further tests were conducted on Zn||Zn symmetric cells with the PBAM-IL-Zn electrolyte under varying current densities. The results demonstrate that cells employing PBAM-IL-Zn can adapt to different current rates. At lower currents such as 0.14 and 0.72 mA cm^{-2}, the amphiphilic ionogel enables stable cycling for over 600 hours (Fig. S8-S9), respectively. Even at a higher current density of 1 mA cm^{-2}, the voltage polarization remains as low as 175 mV after 500 hours of cycling (Fig. S10). This indicates that the amphiphilic ionogel maintains its effectiveness in suppressing zinc dendrites at elevated current densities, a behavior attributed to its unique structure, the functional groups that regulate Zn^{2+} transport, and the properties of the generated SEI layer on the zinc anode.

When tested under more stringent conditions of 2 mA cm^{-2} and 1 mAh cm^{-2}, a Zn||Zn cell with PBAM-IL-Zn exhibited stable operation for 2800 hours with a voltage polarization of 200 mV (Fig. 3h). Post-cycling SEM characterization of the zinc anode revealed a densely packed structure dominated by the (002) crystal plane (Fig. 4a), whereas the anode cycled with PAM-IL-Zn showed pronounced dendritic growth (Fig. 4b). A schematic model illustrating the dendrite-suppression mechanism of the amphiphilic ionogel is proposed in Fig. 4c. The differing solubility of [EMIm]TFSI towards fluorinated monomers/polymers *versus* acrylamide/PAAm induces *in situ* phase separation, forming ion-conducting channels filled with zinc salt. Subsequent introduction of a limited amount of water triggers self-assembly driven by the hydrophilic PAAm and the hydrophobic fluorinated polymer, resulting in a graded pore structure with larger pores on one side and smaller pores on the other. It is worth noting that this gradient structure does not require differentiation in symmetric cells. In full cells, however, due to the zinc-philic nature of PAN, the smaller pores are more likely to form on the zinc anode side. This structure promotes uniform Zn^{2+} flux. Furthermore, the

This journal is © The Royal Society of Chemistry 2026

Published on 07 April 2026. Downloaded by NANJING UNIVERSITY on 5/12/2026 11:44:42 AM.

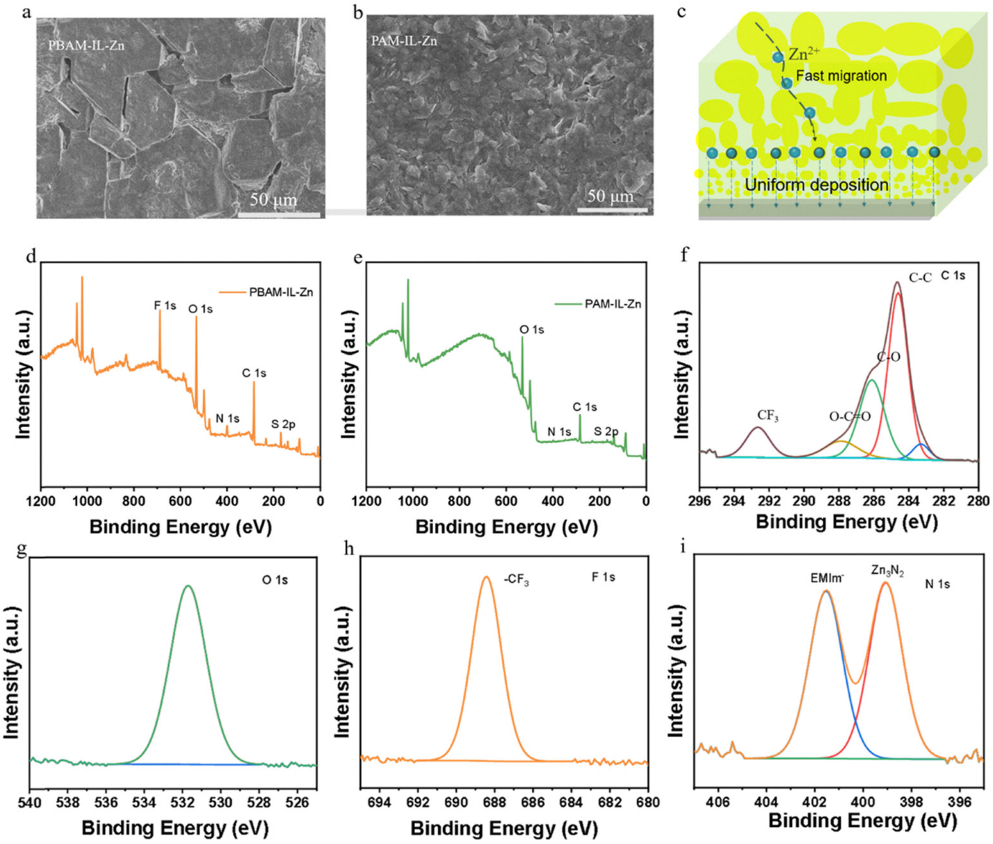

Fig. 4 Morphological characterization, stabilization mechanism, and compositional analysis of zinc anodes. SEM images of zinc electrodes from symmetric Zn||Zn cells using (a) PBAM-IL-Zn and (b) PAM-IL-Zn after long-term cycling at 2 mA cm^{-2} and 1 mAh cm^{-2}. (c) Schematic illustrating the mechanism of zinc dendrite suppression by PAM-IL-Zn. High-resolution X-ray photoelectron spectroscopy (XPS) survey scans of the zinc surface after cycling in symmetric Zn||Zn cells employing (d) PBAM-IL-Zn and (e) PAM-IL-Zn. XPS spectra of (f) C 1s, (g) O 1s, (h) F 1s, and (i) N 1s.

coordinated interactions of Zn^{2+} with fluorine-containing groups and oxygen functionalities, coupled with water immobilization by PAAm-rich segments at the interface, synergistically suppress hydrogen evolution and corrosion, guiding uniform zinc deposition.

XPS analysis was performed on thoroughly washed zinc anodes after cycling. Compared to the anode from the PAM-IL-Zn cell (Fig. 4e), the full survey spectrum for the PBAM-IL-Zn cell (Fig. 4d) shows a distinct F 1s peak and a significantly stronger N 1s signal, indicating these elements are primary constituents of the SEI layer. High-resolution C 1s (Fig. 4f) and O 1s (Fig. 4g) spectra from the PBAM-IL-Zn cycled anode confirm the presence of organic carbon species. While organic carbon and nitrogen species are also detected on the PAM-IL-Zn cycled anode (Fig. S11), the PBAM-IL-Zn anode surface is uniquely rich in organic fluorides (a peak at 688.2 eV assigned to $-CF_3$) and inorganic nitride (a peak at 398.8 eV assigned to Zn_3N_2). Consequently, the PBAM-IL-Zn facilitates the formation of an organic/inorganic hybrid SEI layer comprising organic fluorides and Zn_3N_2 on the zinc anode. The organic fluoride component forms a hydrophobic interface that protects the anode from free water corrosion, while the inorganic Zn_3N_2 component promotes uniform Zn^{2+} deposition and enhances its deposition kinetics. Furthermore, components from the ionic liquid ($[EMIm]^+$) are also present in zinc anode after cyling with PABM-IL-Zn, which is attributed to strong electrostatic interactions with the zinc anode, contributing to a deshielding effect that facilitates uniform Zn^{2+} migration. Notably, the characteristic peak of $[EMIm]^+$ was not detected in the N 1s spectrum (Fig. S11b) of the zinc anode surface after cycling with PAM-IL-Zn. It is speculated that this is attributed to the synergistic effect of the ion–dipole interaction between PBAM-IL-Zn and the ionic liquid, together with the electrostatic adsorption of $[EMIm]^+$ on the zinc anode surface.

To assess the practical application potential of the ionogels, Zn|PBAM-IL-Zn|NVO full cells were assembled and tested at various current densities, with the PAM-IL-Zn serving as a comparison. As shown in Fig. 5a, the Zn||NVO cell employing the PAM-IL-Zn exhibited negligible capacity at 1 A g^{-1}. In contrast, the cell based on PBAM-IL-Zn demonstrated stable rate capability at this current density, with its corresponding charge–discharge profiles presented in Fig. 5b. At a current density of 0.1C (Fig. 5c), the PAM-IL-Zn-based cell maintained a relatively stable Coulombic efficiency for the initial 200 cycles. However, significant efficiency fluctuations emerged upon further cycling, while the discharge capacity remained consistently below 300 mAh g^{-1}. This indicates that the PAM-IL-Zn inadequately facilitates Zn^{2+} migration and fails to suppress

Published on 07 April 2026. Downloaded by NANJING UNIVERSITY on 5/12/2026 11:44:42 AM.

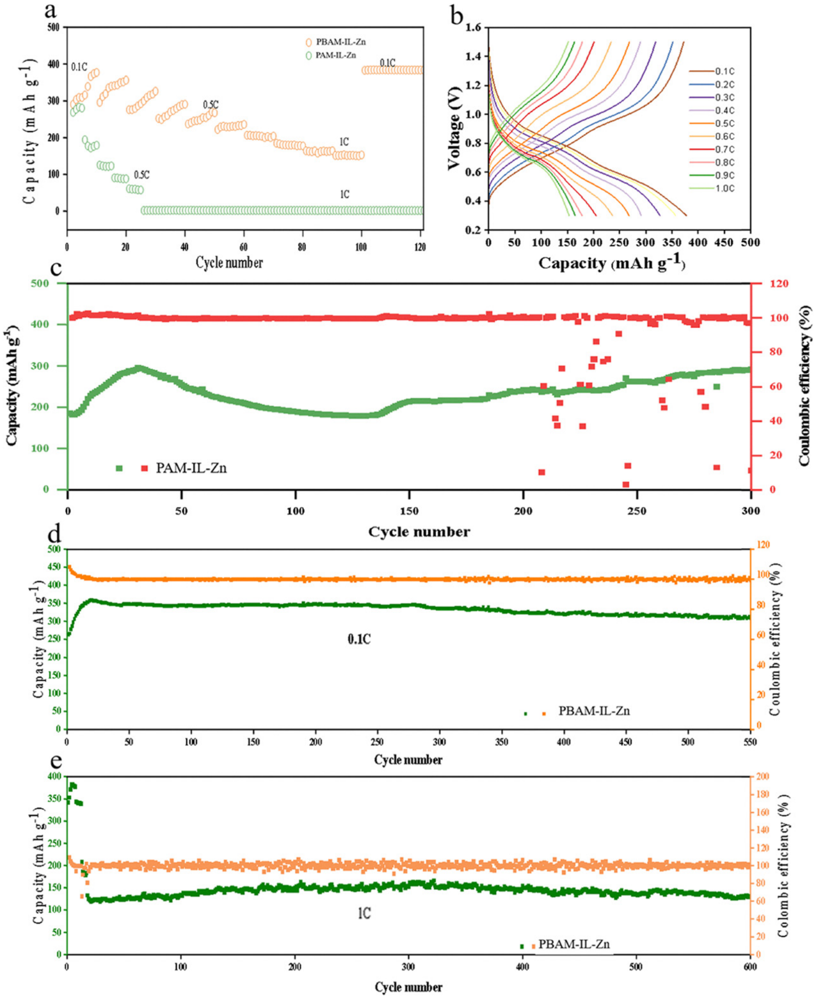

Fig. 5 Full-cell performance. (a) Rate capability of full cells employing PBAM-IL-Zn and PAM-IL-Zn. (b) Charge–discharge profiles of the full cell using PBAM-IL-Zn at various rates. Long-term cycling performance at 0.1C for full cells using (c) PBAM-IL-Zn and (d) PAM-IL-Zn. (e) Long-term cycling performance at 1C for full cells using PBAM-IL-Zn and PAM-IL-Zn.

dendrite growth, leading to internal soft short-circuiting and overcharging during cycling, which consequently results in performance degradation and shortened cycle life. In comparison, the Zn||NVO cell utilizing PBAM-IL-Zn (Fig. 5d) achieved stable cycling for over 550 cycles, with a Coulombic efficiency close to 100% and discharge capacities consistently exceeding 300 mAh g^{-1}, reaching a maximum above 350 mAh g^{-1}. These results further validate the advantages of the amphiphilic ionogel with its unique composition and pore structure, and that the formed organic/inorganic hybrid SEI layer protects the zinc anode, mitigates free-water corrosion, and suppresses side reactions, thereby enabling high capacity and extended cycle life. Furthermore, charging/discharging performance was evaluated for the Zn|PBAM-IL-Zn|NVO cell at a high current density of 1 C (Fig. 5e). The cell sustained stable cycling for 600 cycles under these conditions, maintaining a discharge capacity above 100 mAh g^{-1} with a capacity retention rate approaching 100%, demonstrating excellent rapid charge–discharge performance.

Conclusion

In summary, we have developed a novel amphiphilic ionogel electrolyte that integrates structural and chemical design to address the key failure modes of zinc-metal anodes. The gradient porous framework, arising from controlled phase separation, serves as a physical ion redistributor, homogenizing Zn^{2+} flux before it reaches the electrode interface. The intrinsic amphiphilicity of the polymer further dictates a ''division of labor'' at the zinc surface: hydrophilic domains manage solvation and initial coordination, while hydrophobic domains build a water-deficient interface that mitigates corrosion and hydrogen evolution. This cooperative action is substantiated by the formation of a protective hybrid SEI and a preferential (002) crystallographic orientation of deposited zinc. The resulting electrochemical performance—marked by low overpotential, high Zn^{2+} transference number, and remarkable cycling stability in both symmetric and full-cell configurations—validates the effectiveness of this multifunctional electrolyte strategy.

Published on 07 April 2026. Downloaded by NANJING UNIVERSITY on 5/12/2026 11:44:42 AM.

This study underscores the critical importance of synchronizing bulk ion-transport properties with nanoscale interfacial engineering in electrolyte design. The molecular engineering strategy based on amphiphilic copolymers and gradient pore structures, while demonstrated here for zinc, holds promise for extension to other multivalent metal anodes such as magnesium and aluminum, where similar challenges of dendritic growth and interfacial instability remain critical.

Author contributions

The authors confirm their contributions as follows: Lei Zhang, Shijun Xiao, and Shi Wang conceived the idea and designed the experiments. Lei Zhang, Xurui Rong, Zhiheng Shao, Yong Jiang, Jiajun Hu, and Wenyu Wang conducted the material synthesis, electrochemical measurements, and data analysis. Gangling Chen performed the structural characterizations. Jitao Huang, Qian Wang, Zhong Jin, and Shi Wang supervised the project, provided resources, and contributed to manuscript writing and revision. All authors discussed the results and approved the final version of the manuscript. The authors also thank Professor Yonghua Li at Nanjing University of Posts and Telecommunications for his co-supervision of Shijun Xiao.

Conflicts of interest

There are no conflicts to declare.

Data availability

All relevant data are available from the authors upon request.

Supplementary information includes experimental details and the following figures: S1 (stretched membrane photo), S2 (cross-sectional SEM of PAM-IL-Zn), S3 (FTIR), S4 (transference numbers of control samples), S5 (impedance vs. temperature of control symmetric cells), S6 (Coulombic efficiencies of Zn||Cu cells), S7 (cycling of Zn||Zn cells with different samples), S8–S10 (cycling of symmetric cells with optimal electrolyte), and S11 (XPS of Zn surfaces after cycling with control samples). See DOI: https://doi.org/10.1039/d6mh00453a.

Acknowledgements

This work was supported by the Key Project of Anhui Provincial Education Department (2024AH051409), National Natural Science Foundation of China (U25A20628, 22561160129, 22479074, 22475096, 52533008, 22402146, 22572140), the Equipment Pre-Research and Ministry of Education Joint Fund (8091B02052407), the Fundamental Research Program Key Project of Jiangsu Province (BK20253008), the Natural Science Foundation of Jiangsu Province (BK20240400, BK20241236), the Science and Technology Major Project of Jiangsu Province (BG2024013), the Scientific and Technological Achievements Transformation Special Fund of Jiangsu Province (BA2023037), the Academic Degree and Postgraduate Education Reforming Project of Jiangsu Province (JGKT24_C001), the Key Core Technology Open Competition Project of Suzhou City (SYG2024122), the Open Research Fund of Suzhou Laboratory (SZLAB-1308-2024-TS005), and the Chenzhou National Sustainable Development Agenda Innovation Demonstration Zone Provincial Special Project (2023sfq11). Natural Science Foundation of NJUPT (NY223079, NY224119).

References

1 S.-J. Zhang, J. Hao, H. Wu, Y. Hu, Q. Chen, B. Johannessen, Q. Ma, D. Luo and S.-Z. Qiao, *Nat. Chem.*, 2026, **18**, 266–274.
2 H. Wang, G. Li, J. Fu, Y. Yang, C. Zhang, J. Zhou, X. Cheng, J. Jiang, Q. Huang and H.-Y. Tam, *Nat. Commun.*, 2026, **17**, 1690.
3 X. Zhu, T. Zhang, J. Zhang, X. Zou, X. Li, Z. Li, A. Ge, C. Cao, G. Xu and M. Zhu, *Adv. Mater.*, 2026, **38**, e19057.
4 X. Nie, Y. Yang, J. Hu, D. Yuan, L. Hu and L.-F. Chen, *J. Mater. Chem. A*, 2025, **13**, 41443–41461.
5 X. Zheng, H. Zhu, Z. Wang, H. Yang, R. Li, W. Luo, W. H. Kan, Y. Dai, H. Zhang and J. Wang, *Nat. Nanotechnol.*, 2025, **21**, 95.
6 Z. Ou, M. Zhao, K. Zhu, Z. Liu, S. Yang, H. Zhang, F. Wang and W. Yang, *Angew. Chem., Int. Ed.*, 2025, **65**, e19611.
7 Z. Gong, Q. Meng, Y. Zhao, C. Wang, W. Wang and Z. Pei, *Angew. Chem., Int. Ed.*, 2026, **65**, e23881.
8 M. Zhao, B. Zhang, X. Bai, J. Zhang, X. Chang, L. Hou, H. Huang, S. Wang, Z. Jin and Q. Wang, *Chem. Eng. J.*, 2025, **520**, 166042.
9 B. Li, B. Zhang, X. Bai, J. Zhang, X. Chang, L. Hou, H. Huang, T. Lu, S. Wang and Z. Jin, *Angew. Chem., Int. Ed.*, 2025, **137**, e202503345.
10 S. Wang, J. Li, B. Yang, B. Zhang, Z. Zhang, S. Zhou, Q. Wang, J. Ma and Z. Jin, *Nano Lett.*, 2025, **25**, 5406–5414.
11 C. Liu, B. Zhang, Z. Liang, X. Bai, J. Zhang, X. Chang, L. Hou, H. Huang, Y. Wei and B. Wu, *Chem. Eng. J.*, 2025, **508**, 160900.
12 Y. Xie, Q. Dou, G. Li, Y. Chen and X. Yan, *Energy Mater.*, 2025, **5**, 500025.
13 C. Huang, M. Zhao, C. Xu, Y. Lv, M. Fang, Q. Dong, Y. Xu, Z. Bo and J. Lu, *Angew. Chem., Int. Ed.*, 2025, **137**, e202511410.
14 A. Clarisza, H. K. Bezabh, S.-K. Jiang, C.-J. Huang, B. W. Olbasa, S.-H. Wu, W.-N. Su and B. J. Hwang, *ACS Appl. Mater. Interfaces*, 2022, **14**, 36644–36655.
15 L. Zhang, J. Wu, T. Lu, X. Li, H. Wu, T. Chen, Y. Zhang, J. Wei, M. Hu and X. Zheng, *Chem. Eng. J.*, 2024, **496**, 153815.
16 S. Wang, X. Wu, C. Liu, L. He, S. Li, Y. Miao, M. Cai, Y. Li, Z.-D. Huang and W.-Y. Lai, *Sci. China: Chem.*, 2024, **67**, 3438–3449.
17 J. Li, A. Azizi, S. Zhou, S. Liu, C. Han, Z. Chang, A. Pan and G. Cao, *eScience*, 2025, **5**, 100294.
18 T. Lu, S. Wang, C. Liu, L. Hou, Y. Wei, Q. Wang and Z. Jin, *Adv. Funct. Mater.*, 2025, e23416.

Published on 07 April 2026. Downloaded by NANJING UNIVERSITY on 5/12/2026 11:44:42 AM.

19 R. Fu, B. Zhang, T. Lu, C. Liu, L. Hou, S. Wang, Y. Ning, Z. Jin and Q. Wang, *Energy Storage Mater.*, 2025, **80**, 104374.

20 Q. Wang, X. He, Y. Liu, Z. Zhang, Y. Zhang, X. Chen, Q. Zhao, M. Chen, Z. Lei and H. Li, *Angew. Chem., Int. Ed.*, 2026, **138**, e20598.

21 L. Qian, H. Zhu, T. Qin, R. Yao, J. Zhao, F. Kang and C. Yang, *Adv. Funct. Mater.*, 2023, **33**, 2301118.

22 G. Yang, J. Huang, X. Wan, B. Liu, Y. Zhu, J. Wang, O. Fontaine, S. Luo, P. Hiralal and Y. Guo, *EcoMat*, 2022, **4**, e12165.

23 Z. M. Liu, X. C. Li, H. Zhang, X. K. Zhang, J. Y. Li, Y. F. Shi, D. X. Geng, Z. L. Li, D. W. Sha, G. X. Yu and C. Yan, *Chem. Eng. J.*, 2025, **519**, 519.

24 J. Cao, F. Zhao, W. Guan, X. Yang, Q. Zhao, L. Gao, X. Ren, G. Wu and A. Liu, *Small*, 2024, **20**, 2400221.

25 Q. Zhang, J. Luan, Y. Tang, X. Ji and H. Wang, *Angew. Chem., Int. Ed.*, 2020, **59**, 13180–13191.

26 K. Wu, J. Huang, J. Yi, X. Liu, Y. Liu, Y. Wang, J. Zhang and Y. Xia, *Adv. Energy Mater.*, 2020, **10**, 1903977.

27 Y. Xu, Y. Peng, X. Xiong, Q. Zhou, B. Peng, T. Wang, S. Eliseeva, Z. Zhu, Y. Ma and R. Holze, *Energy*, 2025, **1**, 100004.

This journal is © The Royal Society of Chemistry 2026